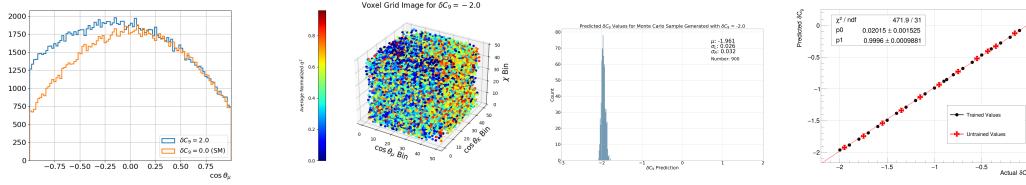


## Graphical Abstract

### Training Deep 3D Convolutional Neural Networks to Extract BSM Physics Parameters Directly from HEP Data: a Proof-of-Concept Study Using Monte Carlo Simulations

S. Dubey, T.E. Browder, S.Kohani, R. Mandal, A. Sibidanov,  
R. Sinha



## Highlights

### **Training Deep 3D Convolutional Neural Networks to Extract BSM Physics Parameters Directly from HEP Data: a Proof-of-Concept Study Using Monte Carlo Simulations**

S. Dubey, T.E. Browder, S.Kohani, R. Mandal, A. Sibidanov,  
R. Sinha

- Transform angular and kinematic distributions into “quasi-images”.
- Train a 34-layer Residual Neural Network to regress on the images and obtain information about the Wilson Coefficient  $C_9$  in  $B \rightarrow K^* \mu^+ \mu^-$  decays.

# Training Deep 3D Convolutional Neural Networks to Extract BSM Physics Parameters Directly from HEP Data: a Proof-of-Concept Study Using Monte Carlo Simulations

S. Dubey<sup>a,1</sup>, T.E. Browder<sup>b</sup>, S.Kohani<sup>b</sup>, R. Mandal<sup>c</sup>, A. Sibidanov<sup>b</sup>,  
R. Sinha<sup>b</sup>

<sup>a</sup>*Department of Physics, Brown University, 182 Hope St., Providence, Rhode Island  
02912, USA*

<sup>b</sup>*Department of Physics and Astronomy, University of Hawai‘i at Mānoa, 2505 Correa  
Rd., Honolulu, HI 96822, USA*

<sup>c</sup>*Indian Institute of Technology Gandhinagar, Department of Physics, Gujarat  
382355, India*

---

## Abstract

We report on a novel application of computer vision techniques to extract beyond the Standard Model (BSM) parameters directly from high energy physics (HEP) flavor data. We develop a method of transforming angular and kinematic distributions into “quasi-images” that can be used to train a convolutional neural network to perform regression tasks, similar to fitting. This contrasts with the usual classification functions performed using ML/AI in HEP. As a proof-of-concept, we train a 34-layer Residual Neural Network to regress on these images and determine the Wilson Coefficient  $C_9$  in MC (Monte Carlo) simulations of  $B \rightarrow K^* \mu^+ \mu^-$  decays. The technique described here can be generalized and may find applicability across various HEP experiments and elsewhere.

*Keywords:* Machine Learning, Neural Networks, Convolutional Neural Networks, CNN, ResNet, Computer Vision, Deep Learning, High Energy Physics, FCNC, Flavor Physics, Effective Field Theories, Wilson Coefficients

---

## 1. Introduction and Motivation

The process  $B \rightarrow K^* \ell^+ \ell^-$  with  $\ell = e, \mu$  proceeds via a beauty-to-strange quark ( $b \rightarrow s$ ) flavor-changing neutral current, which is forbidden at tree-level in the Standard Model (SM) of particle physics but allowed at second order [1]. It is therefore sensitive to beyond the Standard Model (BSM) physics.

Lepton flavor universality, which is the equal coupling of all lepton flavors ( $e, \mu, \tau$ ) to the weak interaction is expected to hold in the Standard Model of particle physics. A deviation from equal coupling would be a signature of lepton flavor universality violation (LFUV), a BSM physics signature. Several flavor physics experiments have previously measured such a deviation from muon-electron universality [2, 3, 4], for  $B \rightarrow K \ell^- \ell^+$  and  $B \rightarrow K^* \ell^+ \ell^-$  in the intermediate  $q^2 \equiv M^2(\ell^+ \ell^-)$  region. However, LHCb's most recent measurements are consistent with the SM [5].

Nevertheless, there are hints of deviations from the SM in the observed angular distributions of  $B \rightarrow K^* \ell^+ \ell^-$ . These can be more clearly identified in angular asymmetries, such as the forward-backward asymmetry ( $A_{FB}$ ),  $S_5$ , and others, described in Ref. [3]. It is possible that these angular asymmetries are lepton-flavor violating. A Belle analysis first directly explored this possibility [4]. It is also possible that BSM physics is lepton-flavor universal (LFU). In the future, determining the scenario from which these apparent anomalies originate — via SM interactions with unaccounted-for hadronic effects, or BSM physics — is a key experimental problem.

Rates and binned angular asymmetries in  $B \rightarrow K^* \ell^+ \ell^-$  are measured and used as input to theoretical fitting packages. These packages [6, 7, 8, 9], construct a  $\chi^2$  from the external measurements and are used to determine BSM physics parameters or deviations from the SM Wilson coefficients, parameters of an effective field theory (EFT) for weak interactions of heavy quarks.

In 2023, the results from the fitting packages still indicate a  $\sim 3\sigma$  hint for BSM physics in the Wilson coefficient  $C_9$  based on the one-dimensional angular asymmetries in  $B \rightarrow K^* \mu^+ \mu^-$ . Further investigations of this type of BSM physics will continue in the future and are discussed below.

In this paper we report on a proof-of-concept method using the Residual Neural Network (ResNet) variation of the convolutional neural network (CNN) [10, 11] to determine BSM physics parameters directly from simulated data. As such, we recast the  $C_9$  determination as a computer vision

problem. To this end, we employ a Monte Carlo (MC) simulation model to generate  $B^0 \rightarrow K^{*0} \mu^+ \mu^-$  events, according to various BSM scenarios parameterized by Wilson coefficients ( $C_i$ ) [12, 13]. From the resulting distributions we create “quasi-images”, which are then used to train a ResNet to perform a regression task.

Our approach differs from the more typical application of artificial intelligence methods in HEP, which involves classification to distinguish various categories of events such as signal versus background; jet classification; or particle identification (determining particle species) etc [14]. In contrast, we will perform regression and extract a continuous parameter from data. This is similar to “fitting”, a different but essential part of HEP analysis. We apply regression and extract the parameter  $\delta C_i \equiv \delta C_i^{\text{BSM}} - \delta C_i^{\text{SM}}$ , where  $\delta C_i = 0.0$  is the SM case. Our neural network model learns the correlation between these images and their  $\delta C_9$  labels, which is equivalent to learning the mapping between the distributions and the  $\delta C_9$  labels. Our MC result is an example of extracting physics parameters directly from detector data. We note that the method presented here may be find broad applicability even in the absence of LFV BSM physics.

Other techniques to extract WCs or effective couplings using AI/ML have been used or proposed for LHC experiments. These usually involve template fitting of neural network outputs or Bayesian inference, etc. Our method using the full four-dimensional distribution of the event sample with a CNN model is different from these approaches [14, 15, 16].

## 2. Monte Carlo Simulation Model

Recently, we have implemented EFT couplings in a new MC generator [12] in the EvtGen framework [17]. The new MC generator uses the operator product expansion formalism in terms of Wilson Coefficients (WCs, which encode high energy/short distance physics information)  $C_7, C_9, C_{10}, C'_7, C'_9,$  and  $C'_{10}$ , where the latter three primed WCs correspond to right-handed couplings (the weak couplings in the SM are usually left-handed).

Our EvtGen model can be parameterized in terms of the WC’s deviation from their SM values, i.e.  $\delta C_i$ . Each of the  $\delta C_i$  can be chosen by the user [12]. Choosing a non-zero  $\delta C_i$  has the effect of altering the correlations between four variables:  $q^2$ , defined previously, the cosine of the lepton helicity angle  $\cos \theta_\ell$ , the cosine of the helicity of the  $K^*$ ,  $\cos \theta_{K^*}$ , and the angle  $\chi$  between the decay planes of the di-lepton and  $K^*$  decay planes. Figure 1 shows the

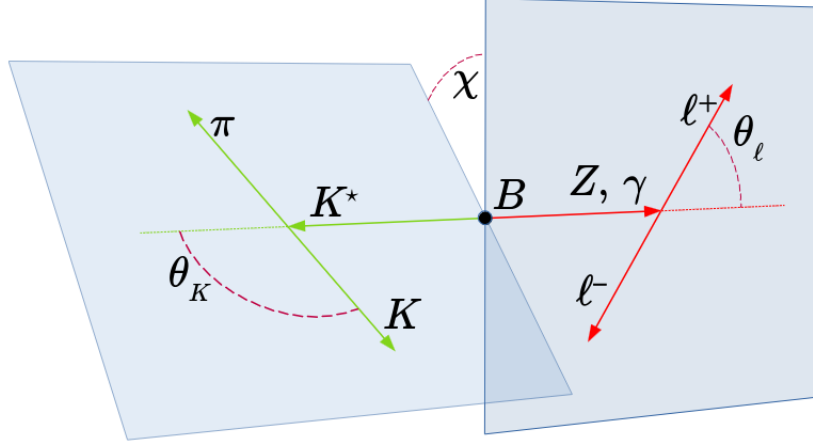


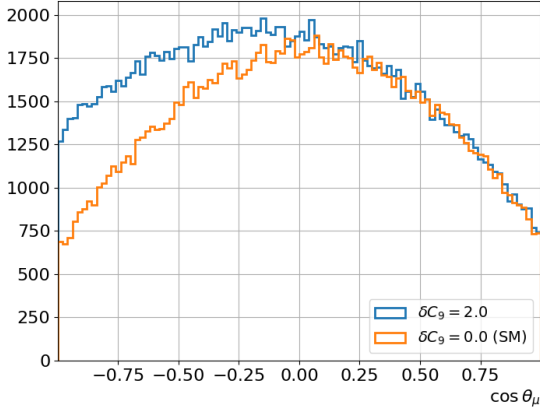
Figure 1: The  $B \rightarrow K^* \ell^+ \ell^-$  decay topology showing the observables [12]. For this study we only consider the di-muon channel.

decay topology and the full set of angular observables while Figure 2 shows examples of their distributions for two different values of  $\delta C_9$ . Distributions are shown for  $1.0 < q^2 < 6.0 \text{ GeV}^2/c^4$ , as that is where the new physics effects are most apparent.

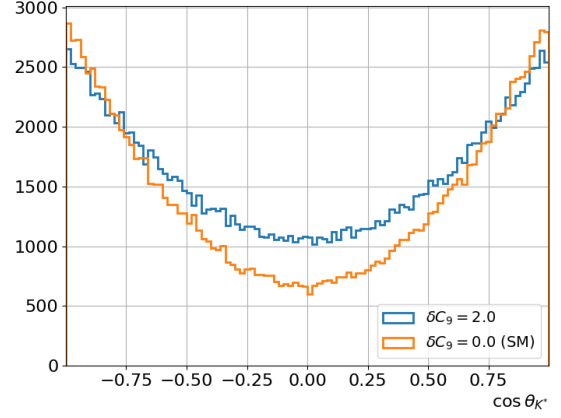
### 3. Creating the Images

As described in Sec. 2, we employ an MC event generator to produce  $B^0 \rightarrow K^{*0} \mu^+ \mu^-$  events. For simplicity, we only consider the  $C_9$  WC, the coupling of the vector term of the model implemented in Ref. [12]. While we are interested in the region where  $\delta C_9 \leq 0.0$ , as theory fits seem to favor a negative  $\delta C_9$  near  $-0.9$  for the di-muon channel [6], samples of MC events are generated with  $\delta C_9 \in [-2.0, 1.1]$ . This is to allow the NN to better learn the physics near  $\delta C_9 = 0.0$ . Twenty-two values are chosen in the above range and  $500 \times 10^3$  events are generated for each of the  $\delta C_9$  values. Only MC events for  $B^0 \rightarrow K^{*0} \mu^+ \mu^-$  are used and not charge conjugate events, as some of the angular asymmetries inherent in the angular distributions that allow for discrimination between SM and BSM physics would cancel, if the charge conjugated events are included in the same images.

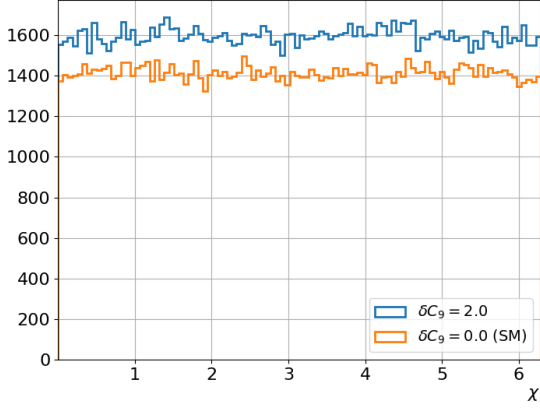
As this is a proof-of-concept study, (quasi-)images are produced with high statistics. Approximately  $2.4 \times 10^4$   $B^0 \rightarrow K^{*0} \mu^+ \mu^-$  events populate a single image. This corresponds to approximately  $250 \text{ ab}^{-1}$ -equivalent integrated



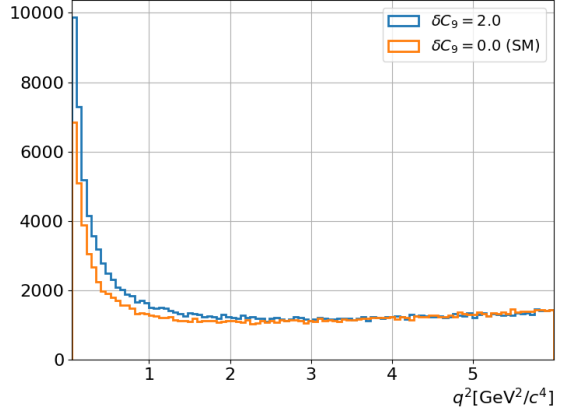
(a)  $\cos \theta_\mu$  Distributions



(b)  $\cos \theta_{K^*}$  Distributions

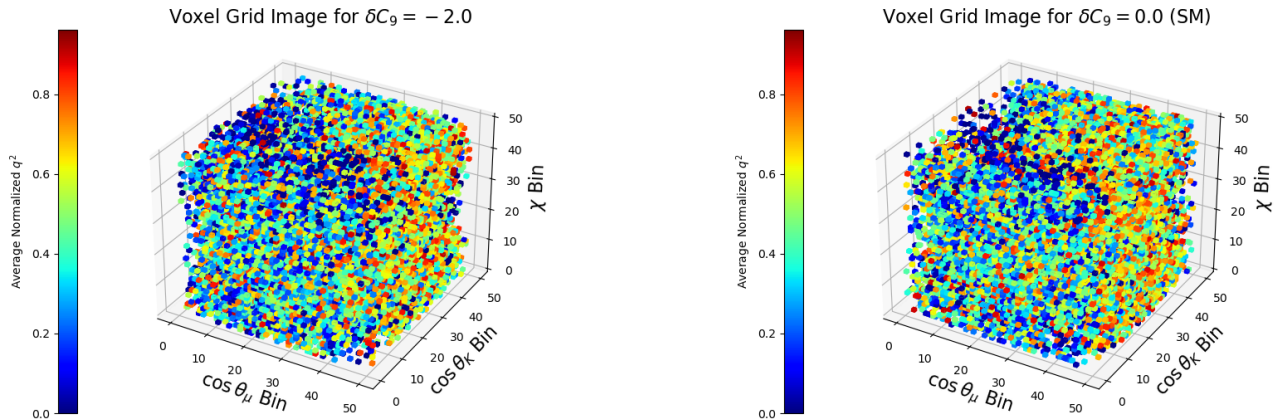


(c)  $\chi$  Distributions



(d)  $q^2$  Distributions

Figure 2: Distributions of the angular and  $q^2$  distributions. Distributions are shown for  $1.0 < q^2 < 6.0 \text{ GeV}^2/c^4$ , as that is where the new physics effects are most apparent. The  $q^2$  values are binned in bins of the angles to create 3D histograms. These are input to the convolutional neural network and treated as voxel grid images to perform regression and find the correlations between these distributions and  $\delta C_9$  values. Two example values are given for each distribution:  $\delta C_9 = 0.0$  (SM) and  $\delta C_9 = -2.0$  (a particular EFT BSM parameterization).



(a) Voxel grid image for  $\delta C_9 = -2.0$

(b) Voxel grid image for  $\delta C_9 = 0.0$  (SM)

Figure 3: Voxel grid images used for training and evaluation of the ResNet. Each angular bin is a range of angular values. The angular range is divided into 50 equal-width bins. Examples for the cases of  $\delta C_9 = 0.0$  (SM) and  $\delta C_9 = -2.0$  are shown. The color of the voxels does not indicate that the image has multiple color channels and is only used for visualization.

luminosity at a Belle II upgrade (assuming the Belle signal reconstruction efficiency of approximately 25%, given in [4]), five times the Belle II target integrated luminosity.

Images are then produced by binning the  $q^2$  value of each event in bins of  $\cos \theta_\mu$ ,  $\cos \theta_{K^*}$ , and  $\chi$ , previously shown in Fig. 2. The whole range of  $q^2$  for  $q^2 \leq 20.0 \text{ GeV}^2/c^4$  is used. There are 50 bins in each angular variable. If there are multiple events in a bin, the average  $q^2$  value in that bin is taken. Therefore, the shape of the input image is (height, width, depth) = (50, 50, 50). In effect, we have created a grid of voxels (3D pixels). We treat the  $q^2$  values as grayscale values, so that the images are input as tensors to the neural network and each have shape (50, 50, 50, 1), where the value 1 denotes the number of color channels.

We note that we produce only generator-level MC signal events to populate the images, i.e. we do not yet include backgrounds, efficiencies, or detector resolution. Figure 3 shows two examples of these images for different values of  $\delta C_9$ .



## 4. The Neural Network

As discussed above, a ResNet variation of the CNN, is employed. ResNets were developed to better train deep neural networks and may help solve problems like vanishing gradients in deep neural networks <sup>1</sup>, where the gradient shrinks during backpropagation, making it difficult for the network to learn [11]. ResNets solve this problem by introduction of a “skip” or “shortcut” connection. These connections send the signal that comes into a layer also directly to a layer further up the network. This forces the model not to learn the underlying function, but rather the residual between the input and the underlying function. A topology chart, provided by Keras [18], of part of the ResNet implemented here is shown in Fig. 4. Each cell in the flow chart has two rows: the top row contains the layer label on the left and the input shape of the input tensor on the right. The bottom row contains the type of layer and the output shape of the tensor. The shapes are given in Python form, where the “None” value means the layer can operate on a batch size that can change. The next three values are the height, width, and depth. Descriptions of the different type of layers used and their effect on the tensors and their dimensions are given in Ref. [11].

Specifically, a three-dimensional variation of the ResNet introduced in Ref. [10] is used and built using TensorFlow [19] and Keras [18]. At the bottom of the network, there are an input layer; a convolutional layer with 64 filters, a kernel size of 7, and a stride of 2; a batch normalization layer followed by a ReLU activation function; and a max pooling layer with a pool size of 3 and a stride of 2. There are 34 convolutional layers in the main neural network path, utilizing the ReLU activation function [11] and SAME padding. Stochastic gradient descent is used for optimization. The loss function is the mean absolute error (MAE) [11]. At the top of network there is a global average pooling layer; a flatten layer; and one fully-connected layer employing 1000 neurons, followed by a dropout layer with a 50% dropout probability. The final layer is a dense layer with one neuron and a linear activation function that performs the regression task to extract  $\delta C_9$  values directly from image test set <sup>2</sup>. No hyperparameter optimization was done as

---

<sup>1</sup>A deep neural network here is one with more than two hidden layers that contain trainable parameters.

<sup>2</sup>The linear activation function is used as its range is a continuum of values in  $(-\infty, \infty)$ .

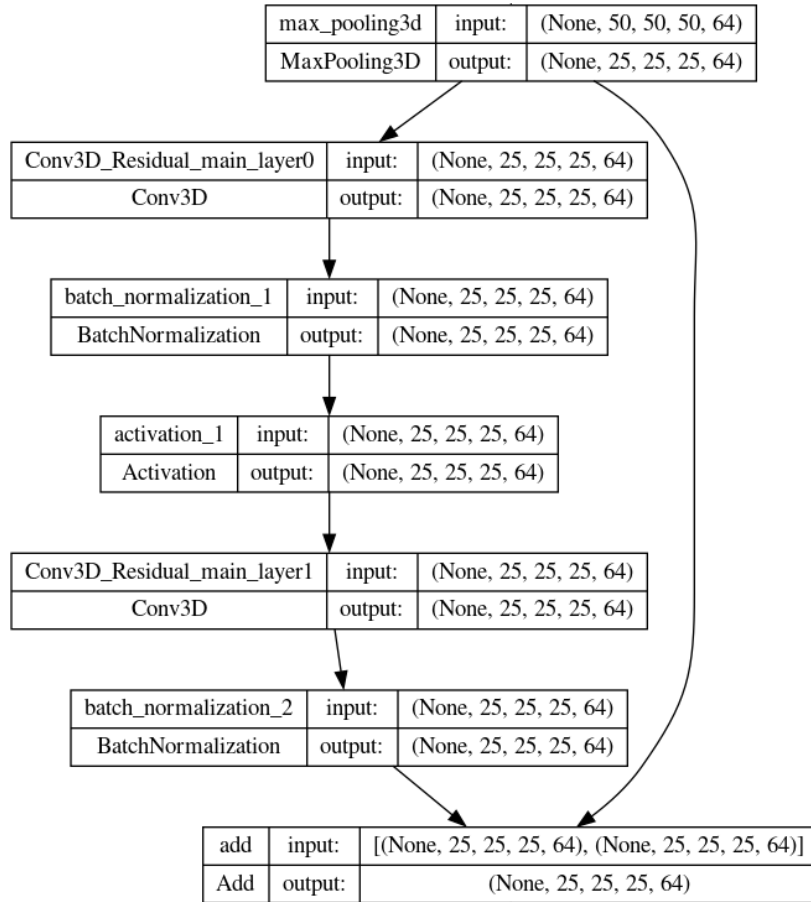


Figure 4: A portion of the topology showing the layers and the skip connection, produced by Keras [11, 18]. The skip connection feeds the input directly into the output and adds them. This prompts the neural network to learn the function residual and may help mitigate issues with deep neural network training, such as vanishing gradients.

the network performance initially worked well.

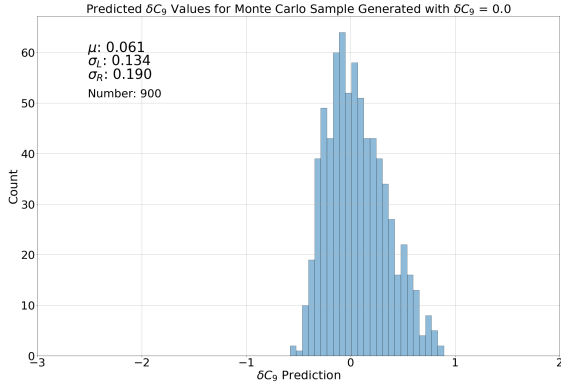
## 5. Training the Neural Network

Voxel grid images are generated for  $\delta C_9 \in [-2.0, 1.1]$ . Due to different MC generation campaigns, the number of voxel grid images per  $\delta C_9$  value is unbalanced. For  $\delta C_9 \in [-2.0, 0.0]$ , the number of voxel grid training images is 2640 in the training set and 720 for the validation set, except for  $\delta C_9 = -0.9$  and  $\delta C_9 = -0.4$ , for which there are 5280 voxel grid images in the training set and 1440 in the validation set. For  $\delta C_9 \in [0.1, 1.1]$  there are 2340 voxel grid images in the training set and 540 in the validation set. A batch size of 128 voxel grid images is used during training.

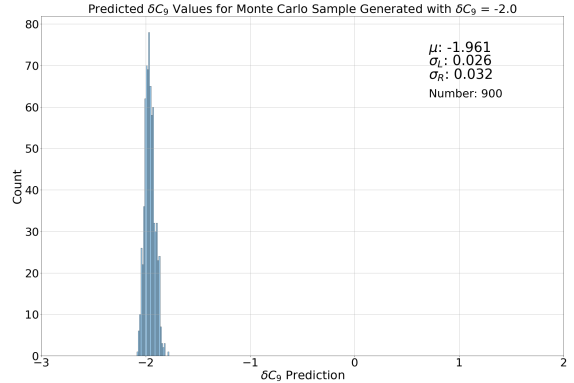
To facilitate learning, the learning rate is reduced every five epochs by a factor of 1/5. Early stopping is implemented if there is no improvement in the validation loss (MAE) after 20 epochs. Training is then performed using the GPU nodes of the University of Hawai‘i’s MANA HPC cluster, using the Slurm job scheduler [20]. The relevant code for the NN, MC generation, voxel grid generation and visualization, training, test set evaluation may currently be found in Ref. [21].

## 6. Results

As this is a AI/ML model for regression and not classification, standard tools to assess the trained model used in classification, e.g. the Receiver Operating Characteristic (ROC) curve [11], are not applicable here. Instead to test the model, we examine ensembles of MC simulation experiments. For each of the 22 WCs that were used to generate training images, statistically independent samples of 900 images are generated as a test set. Each of the ensembles of 900 images are passed through the trained network and a distribution of predicted  $\delta C_9$  values are obtained. We also generate 900 images using  $\delta C_9$  values that are between the ones used to generate the training images. This provides a further test of model robustness as it is a test of the model’s ability to predict  $\delta C_9$  values for images for which the model has not been explicitly trained. Examples of these prediction distributions are provided in Fig. 5. Using the Pandas software [22, 23], these distributions are used to calculate a mean ( $\mu$ ), and a left ( $\sigma_L$ ) and right ( $\sigma_R$ ) standard deviation, as these distributions are not symmetric, in general.



(a) Voxel grid image for  $\delta C_9 = 0.0$  (SM)



(b) Voxel grid image for  $\delta C_9 = -2.0$

Figure 5: Fits to predictions for an ensemble of 900 independent images that were reserved for testing. We generate ensembles different  $\delta C_9$  values. The output distributions of the ResNet are fitted with a Gaussian function and the fitted parameters are used for model assessment. The y-axis gives the bin count.

The predicted results from the NN are plotted against their actual values to obtain a linearity plot, given in Fig. 6. The error bars are scaled by  $\sqrt{N}$ , where  $N$  is the number of test images in the MC ensemble for each  $\delta C_9$  value ( $N = 900$ ). Figure 7 plots the same points with their unscaled error bars to provide the sensitivity based on the NN and the test set MC ensemble. As global theory fits for the dimuon-specific  $\delta C_9$  appear to favor a negative value near  $-0.9$  [6], we consider only values for  $\delta C_9 \leq 0.0$  in Fig. 6 and Fig. 7.

## 7. Discussion

As seen in the linearity plot in Fig. 7, the ResNet appears to be able to obtain a mapping between  $\delta C_9$  values and MC signal events when those events are recast into images. However, as one approaches the SM  $\delta C_9 = 0.0$  value, performance degrades. This is because the images closer to the SM are harder to distinguish, as BSM contributions here can be smaller. Further, when compared to the results of the 4D unbinned maximum likelihood fit to generator-level signal MC samples in Ref. [12], the upper error bar ( $\sigma_R$ ) from the ensemble test for  $\delta C_9 = 0.0$  is 2.6 times larger, at  $250 \text{ ab}^{-1}$ -equivalent signal events. Nevertheless, we do not interpret this as a major defect for the

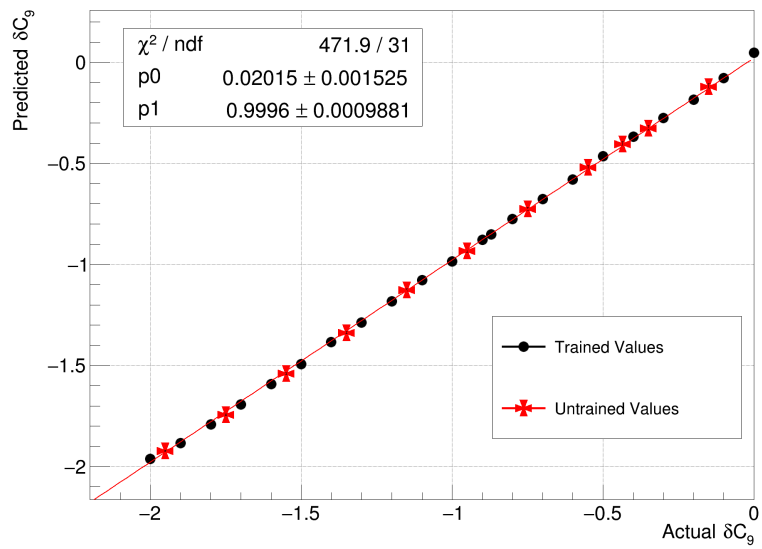


Figure 6: Linearity test from the MC ensemble experiments. Black circles are from MC ensemble experiments in which images are generated using  $\delta C_9$  values that the model had seen in training. Red crosses are from MC ensemble experiments where images are generated using  $\delta C_9$  values that the model had not seen in training. The error bars are scaled by  $\sqrt{N}$ , where  $N$  is the number of test images in the MC ensemble for each  $\delta C_9$  value ( $N = 900$ ).

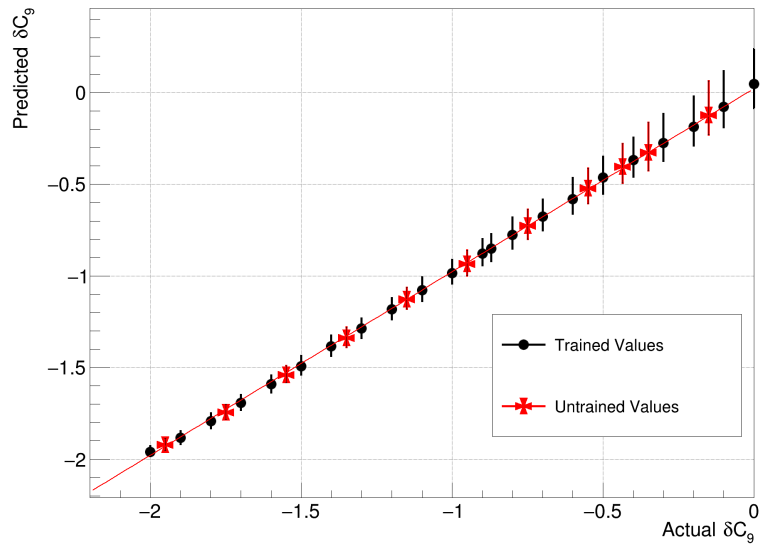


Figure 7: Results from the MC ensemble experiments. Black circles are from MC ensemble experiments in which images are generated using  $\delta C_9$  values that the model had seen in training. Red crosses are from MC ensemble experiments where images are generated using  $\delta C_9$  values that the model had not seen in training. The lower error bar is  $\sigma_L$  and the upper error bar is  $\sigma_R$ , which are determined from the test set prediction distributions.

method presented here. These issues are likely to be ameliorated with more training data.

Further, using a 4D unbinned maximum likelihood fit has a number of problems in a real high energy physics experiment. In the presence of backgrounds and resolutions, it is difficult to parameterize the backgrounds, efficiency, and resolution in multiple dimensions. The associated issues may be greatly mitigated if the problem is recast as a computer vision problem.

The main issue with the method described here is one of computational power and storage. We used  $\delta C_9$  and high-statistics generator level MC samples for the demonstration. In reality, a fully trained and useful model would have to be trained using images according to all the WCs mentioned above, as well as different integrated luminosities (assuming applicability at Belle II).

As an initial naive approach, prior to this study, we attempted to train a fully-connected neural network [11] using the angular and  $q^2$  values of one  $B$  ( $\bar{B}$ ) decay event, as one training instance. This approach did not yield a neural network that was able to learn to map the kinematic input values to a  $\delta C_9$  output value. This is likely due to the fact that such a NN has difficulty finding correlations on an event-by-event basis due to the subtle differences in the distributions. This is why recasting the problem as a computer vision problem appears to be effective: many events are used to create a single image (i.e. a single training instance), and having many events in a single training instance makes the correlations between the angular and  $q^2$  distributions, and  $\delta C_9$  values, more apparent.

## 8. Conclusion

We have trained a three-dimensional ResNet to learn a mapping between different  $\delta C_9$  values and images, created using kinematic distributions obtained from MC simulations of  $B \rightarrow K^* \ell^+ \ell^-$  decays. We have recast the problem of fitting complicated multi-dimensional distributions using maximum likelihood techniques as a standard computer vision problem. This should make it relatively easy to take into account experimental complexities such as backgrounds and experimental resolutions and does not require projecting down to a lower dimension (e.g. in this case to angular asymmetries such as  $A_{\text{FB}}$  and  $S_5$ ), losing potentially valuable information. Our approach may also find application to studies of  $\bar{B}^0 \rightarrow D^{*+} \ell^- \bar{\nu}$ , where a new BSM physics generator has also recently been developed [24].

We have shown that a ResNet is indeed able to learn a correlation and successfully extract information about a relevant physics parameter. Difficulties with this method will likely be mitigated with increased training sample sizes and additional computational resources.

This CNN-based regression method is quite general. While we have performed our study with an eye toward Belle II and flavor physics experiments, it should be applicable to other areas of high energy physics. For example, it may find relevance in the study of  $t\bar{t}H$  or  $WWZ$  couplings at CMS and ATLAS, which has already commenced using machine learning approaches [25]. In general, we hope to provide a more efficient and flexible method of performing BSM physics searches that are broadly applicable across different fields of physics.

A preliminary version of the results described above were presented in a poster during the 2023 Computing in High Energy Physics conference in Norfolk, Virginia and are briefly discussed in the Proceedings. This work supersedes that.

## 9. Acknowledgements

We thank our colleagues on Belle II as well as the KEK computing group for their excellent operation of the KEK computing center. We have used the University of Hawai'i MANA HPC cluster. The technical support and advanced computing resources from University of Hawai'i Information Technology Services – Cyberinfrastructure, funded in part by the National Science Foundation CC\* awards # 2201428 and # 2232862 are gratefully acknowledged. We also thank Hongyang Gao (ISU) for his seminal suggestion to use computer vision techniques to search for new physics couplings, and Chunhui Chen (ISU) for facilitating the meeting, as well as Peter Sadowski (UHM), Jeffrey Schueler (UNM) and Sven Vahsen (UHM) for their helpful discussions on machine learning and technical advice.

## References

- [1] S. L. Glashow, J. Iliopoulos, L. Maiani, Phys. Rev. D 2 (Oct 1970).
- [2] J. P. Lees, et al., Phys. Rev. D 86 (2012) 032012.
- [3] R. Aaij, et al., Journal of High Energy Physics 2017 (8) (2017) 55.



- [4] S. Wehle, et al., Phys. Rev. Lett. 126 (2021) 161801.
- [5] LHCb collaboration, Test of lepton universality in  $b \rightarrow s\ell^+\ell^-$  decays (2022). [arXiv:2212.09152](https://arxiv.org/abs/2212.09152).
- [6] W. Altmannshofer, P. Stangl, New Physics in Rare B Decays After Moriond 2021, The European Physical Journal C 81 (10) (2021) 952.
- [7] M. Algueró, et al., The European Physical Journal C 82 (4) (apr 2022).
- [8] T. Hurth, et al., Physics Letters B 824 (2022) 136838.
- [9] M. Ciuchini, et al. (2022). [arXiv:2110.10126](https://arxiv.org/abs/2110.10126).
- [10] K. He, X. Zhang, S. Ren, J. Sun, Deep Residual Learning for Image Recognition (2015). [arXiv:1512.03385](https://arxiv.org/abs/1512.03385).
- [11] A. Geron, Hands-on machine learning with scikit-learn, keras, and TensorFlow, 2nd Edition, O'Reilly Media, Sebastopol, CA, 2019.
- [12] A. Sibidanov, et al., A New Monte Carlo Generator for BSM physics in  $B \rightarrow K^*\ell^+\ell^-$  decays with an application to lepton non-universality in angular distributions (2022). [arXiv:2203.06827](https://arxiv.org/abs/2203.06827).
- [13] M. D. Schwartz, Quantum Field Theory and the Standard Model, Cambridge University Press, 2013.
- [14] HEP ML Community, A Living Review of Machine Learning for Particle Physics, and references therein.  
URL <https://iml-wg.github.io/HEPML-LivingReview/>
- [15] J. Brehmer, et al., Phys. Rev. Lett. 121 (2018) 111801.
- [16] J. Brehmer, et al., Phys. Rev. D 98 (2018) 052004.
- [17] D. J. Lange, The EvtGen particle decay simulation package, Nucl. Instrum. Meth. A 462 (2001) 152–155.
- [18] F. Chollet, et al., Keras, <https://keras.io> (2015).
- [19] M. Abadi, et al., TensorFlow: Large-scale machine learning on heterogeneous systems, software available from [tensorflow.org](https://www.tensorflow.org) (2015).  
URL <https://www.tensorflow.org/>

- [20] SchedMD, Schedmd/slurm: Slurm: A highly scalable workload manager.  
URL <https://github.com/SchedMD/slurm>
- [21] [https://gitlab.com/sd\\_86/ml4hep/-/tree/main/btokstar11\\_cnn\\_study\\_final](https://gitlab.com/sd_86/ml4hep/-/tree/main/btokstar11_cnn_study_final), [Accessed 20-11-2023].
- [22] The pandas development team, pandas-dev/pandas: Pandas (Feb. 2020). doi:10.5281/zenodo.3509134.  
URL <https://doi.org/10.5281/zenodo.3509134>
- [23] Wes McKinney, Data Structures for Statistical Computing in Python, in: Stéfan van der Walt, Jarrod Millman (Eds.), Proceedings of the 9th Python in Science Conference, 2010, pp. 56 – 61.
- [24] B. Bhattacharya, et al., Phys. Rev. D 107 (2023) 015011.
- [25] N. Tonon, et al., Journal of High Energy Physics 2021 (12) (2021) 83.